Effect of Morphological Defects on Gas Adsorption in Nanoporous Silicas†

4 AUTHORS, INCLUDING:

Anne Galarneau
Institut Charles Gerhardt
154 PUBLICATIONS   4,164 CITATIONS

Francesco Di Renzo
French National Centre for Scientific Research
229 PUBLICATIONS   5,249 CITATIONS

Roland J-M Pellenq
Massachusetts Institute of Technology
215 PUBLICATIONS   3,794 CITATIONS

Effect of Morphological Defects on Gas Adsorption in Nanoporous Silicas[†]

Benoit Coasne,*,[‡] Anne Galarneau,[‡] Francesco Di Renzo,[‡] and R. J. M. Pellenq[§]

Institut Charles Gerhardt Montpellier, UMR 5253 CNRS, Université Montpellier 2, ENSCM, Place Eugène Bataillon, 34095 Montpellier Cedex 05, France, and Centre de Recherche en Matière Condensée et Nanosciences, UPR 7251 CNRS, Campus de Luminy, 13288 Marseille Cedex 09, France

This paper reports a molecular simulation study on the adsorption of a simple fluid in nanoporous silicas with or without morphological defects (constrictions). All of the pores considered in this work are of a finite length and are connected to a bulk reservoir so that they mimic real materials for which the confined fluid is always in contact with the external gas phase. The adsorption isotherms for the regular cylindrical pores conform to the typical experimental behavior for MCM-41 as the adsorbed amount increases continuously in the multilayer adsorption regime until a jump occurs due to capillary condensation of the fluid within the pore. The evaporation pressures are lower than the condensation pressures, so that hysteresis loops are observed. The condensation and evaporation mechanisms for the pores with constrictions depart significantly from what is observed for regular nondefective nanopores. Depending on the size, length, and number of constrictions in the pores, the filling and emptying processes are found to be of different nature. In every case, these mechanisms involve the coexistence between the confined liquid and some gas nanobubbles that are trapped within the main cavities of the pore. It is also found that the finite length of the pore introduces some heterogeneity in the adsorption and desorption processes; the filling and emptying of the regions (constrictions and cavities) near the pore surface differs from those of the regions in the pore center. The desorption process can occur through different mechanisms such as cavitation, pore blocking effects with at equilibrium evaporation, or several combined pore blocking effects. Adsorption isotherms can be used to assess and characterize morphological defects in nanopores. In contrast, our results suggest that microcalorimetry experiments such as measurements of the isosteric heat of adsorption cannot be used to gain information regarding such defects as all of the data for the regular and constricted pores fall on the same curve.

1. Introduction

The behavior of fluids confined within nanometric pores (size of a few molecular diameters) significantly differs from that of the bulk.[1,2] In particular, the effect of confinement, surface forces, and reduced dimension affect the phase transition characteristic quantities (condensation, freezing, etc.). Significant shifts in transitions (e.g., pressure and temperature) are observed, and in some cases, new types of phase transitions (layering, wetting, etc.) can also be found for these inhomogeneous systems. Understanding such confinement and surface effects on the thermodynamics of fluids is of crucial interest for both fundamental research and potential applications.

Among nanoporous solids, the siliceous MCM-41[3] and SBA-15[4] are important materials because of their possible uses as adsorbents or catalytic supports for gas adsorption, phase separation, catalysis, preparation of nanostructured materials, drug delivery, etc.[5−7] These materials are obtained by a template mechanism involving the formation of surfactant or block copolymers micelles in a mixture composed of a solvent and a silica source. After polymerization of the silica and removal of the organic micelles, one obtains a material made up of an array of regular pores. The pore diameter distribution is narrow with an average value that can be varied from 2 up to 20 nm, depending on the synthesis conditions.[7] From a fundamental point of view, MCM-41 and SBA-15 are considered as model materials to investigate the effect of nanoconfinement on the thermodynamic properties of fluids. In particular, the cylindrical geometry of the pores in these materials makes it possible to address in a simple way the effect of confinement on the adsorption, capillary condensation, and freezing and melting of fluids in nanopores. As a result, many experimental, theoretical, and molecular simulation studies have been reported on the thermodynamics of fluids confined in these materials (for reviews, see refs 1 and 2). Properties of MCM-41 and SBA-15 have been extensively studied by combining transmission electronic microscopy (TEM), X-ray diffraction, and adsorption experiments.[5,6] For instance, it has been shown that the cylindrical nanopores in SBA-15 materials are connected through transversal nanoporous channels.[8−12] In addition, Ryoo and co-workers have shown by means of high-resolution TEM that the main pores in SBA-15 exhibit undulations along their axis in order to smooth the heterogeneities induced by the interconnecting channels.[13] On the other hand, it is generally agreed that MCM-41 is made up of unconnected nanopores.[9,14] Despite the significant amount of information gained on the properties of these materials, some uncertainties remain regarding their surface chemistry (presence of impurities, defects, etc.) as well as their surface texture (microporosity, surface roughness, and existence of defects such as constrictions).[15−17]

[†] Part of the "Keith E. Gubbins Festschrift".

* To whom correspondence should be addressed. E-mail: bcoasne@lpmc.univ-montp2.fr. Phone: +33 4 67 14 33 78. Fax: +33 4 67 14 42 90.

[‡] Institut Charles Gerhardt Montpellier.

[§] Centre de Recherche en Matière Condensée et Nanosciences.

TABLE 1: Morphological Properties of the Regular (pores A1 and A2) and Constricted (pores B1, B2, B3, and B4) Nanopores Considered in This Work[a]

porous material	diameter D in nm (length L in nm)						
	Regular Pores						
pore A1	3.2 (25.6)						
pore A2	6.4 (25.6)						
	Constricted Pores						
pore B1	3.2 (1.1)	6.4 (6.4)	3.2 (2.1)	6.4 (6.4)	3.2 (2.1)	6.4 (6.4)	3.2 (1.1)
pore B2	4.8 (1.1)	6.4 (6.4)	4.8 (2.1)	6.4 (6.4)	4.8 (2.1)	6.4 (6.4)	4.8 (1.1)
pore B3	3.2 (1.1)	6.4 (23.4)	3.2 (1.1)				
pore B4	3.2 (1.1)	6.4 (6.4)	3.2 (10.7)	6.4 (6.4)	3.2 (1.1)		
pore B5	3.2 (9.6)	6.4 (6.4)	3.2 (9.6)				

[a] Numbers provide the sequence of cavity and constriction diameters D starting from one of the pore opening. For each cavity or constriction, the number in parentheses corresponds to its length L. For example, $D_p(L_p) - D_c(L_c)$ corresponds to a cavity of a diameter D_p and a length L_p followed by a constriction of a diameter D_c and a length L_c. For all systems, the total length of the pore is 25.6 nm.

The aim of the present work is to investigate by means of grand canonical Monte Carlo (GCMC) molecular simulation, the behavior of a simple fluid (argon) confined within atomistic silica nanopores MCM-41, that is, pore models described at the atomistic level where all of the atoms are explicitly taken into account. Two models of cylindrical silica nanopores MCM-41 are considered. Model A is a regular cylindrical pore of a finite length that is opened at both ends toward an external bulk reservoir. For this reference system, we consider two different pore diameters, $D = 3.2$ nm and $D = 6.4$ nm. Model B is a cylindrical pore of a finite length having undulations (smooth defects) or constrictions (more severe defects). We address the effect of the size of these defects by varying their length and diameter. We also consider the effect of the number of constrictions and undulations. We emphasize that all of the pores considered in this work are of a finite length and connected to bulk reservoirs so that they mimic real materials for which the confined fluid is always in contact with the external gas phase (this departs from infinitely long pores for which the evaporation of the confined liquid necessarily occurs through cavitation as there is no interface with the external phase). The comparison between models without (model A) and with (model B) defects allows us to discuss the effect of such morphological defects on the adsorption and desorption mechanisms. For a pore with constrictions, the desorption occurs either through "pore blocking" effects or "cavitation". In a desorption process that occurs through pore blocking, the confined liquid only evaporates when the constriction, which isolates the pore from the gas, empties.[18,19] In contrast, cavitation corresponds to an evaporation process that consists of the nucleation of a gas bubble within the pore while the constrictions remain filled by the liquid. For characterization purposes, the aim of the present work is to determine the relevance of the information that is assessed from adsorption-based measurements (adsorption isotherm, calorimetry, etc.) in the case of pores having morphological defects. In particular, we address the relevance of the pore sizes and morphological features that are estimated from the capillary condensation and evaporation pressures.

2. Methods

2.1. Pore Models. The atomistic pores used in this work were generated according to the method proposed by Pellenq and Levitz to prepare numerical Vycor samples.[20] Coasne and Pellenq have shown that this technique can be used to prepare pores of various morphologies and topologies, such as cylindrical, hexagonal, ellipsoidal, and constricted pores.[21-23] For each pore model, the porous network can be defined using a mathematical function $\eta(x,y,z)$ that equals 1 if (x,y,z) belongs to the pore wall and 0 if (x,y,z) belongs to the pore void. The

pore models used in this work were obtained by carving out of an atomistic block of cristobalite (cristalline silica) the porous network corresponding to $\eta(x,y,z) = 0$. In order to mimic the pore surface in a realistic way, we removed in a second step the Si atoms that are in an incomplete tetrahedral environment. We then removed all oxygen atoms that are nonbonded. This procedure ensures that the remaining silicon atoms have no dangling bonds and the remaining oxygen atoms have at least one saturated bond with a Si atom. Then, the electroneutrality of the simulation box was ensured by saturating all oxygen dangling bonds with hydrogen atoms. The latter are placed in the pore void, perpendicularly to the pore surface, at a distance of 1 Å from the closest unsaturated oxygen atom. Then, we displace slightly and randomly all of the O, Si, and H atoms in order to mimic an amorphous silica surface (the maximum displacement in each direction x, y, and z is 0.7 Å). It has been shown[20] that the density of OH groups obtained using such a procedure (7 OH per nm²) is close to that obtained experimentally for porous silica glasses such as Vycor (5−7 OH per nm²).[24,25] On the other hand, the density of OH groups at the surface of real MCM-41 is usually smaller, 2 or 3 OH per nm².[26−30] Despite this quantitative difference in the surface chemistry of the numerical and real samples, it has been shown that the simulated materials obtained using the procedure described above are able to capture the adsorption and condensation of fluids in nanoporous silicas.[20,22,23] Moreover, the discussion on the effect of the existence of morphological defects by comparing the simulations for regular and constricted silica pores is relevant since the surface chemistry is the same for all samples.

We considered two models of cylindrical silica nanopores. Model A is simply a regular cylindrical pore of a finite length that is opened at both ends toward an external bulk reservoir. Model B is a cylindrical pore of a finite length having constrictions. The properties of the different pores considered in this work for model A and B are reported in Table 1. We also report in Figures 1 and 2 transversal views of the silica pores without and with constrictions. For all pores, the total length is 25.6 nm. For model A, two pore diameters have been considered, $D = 3.2$ nm and $D = 6.4$ nm (pore A1 and pore A2). For model B, we prepared four pores with different constriction length, size, and number (pores B1, B2, B3, B4, and B5).

2.2. Grand Canonical Monte Carlo. We performed GCMC simulations of argon adsorption at 77 K in the atomistic models of silica nanopores with and without constrictions. The GCMC technique is a stochastic method that simulates a system having a constant volume V (the pore with the adsorbed phase), in equilibrium with an infinite reservoir of particles imposing its

Gas Adsorption in Nanoporous Silicas

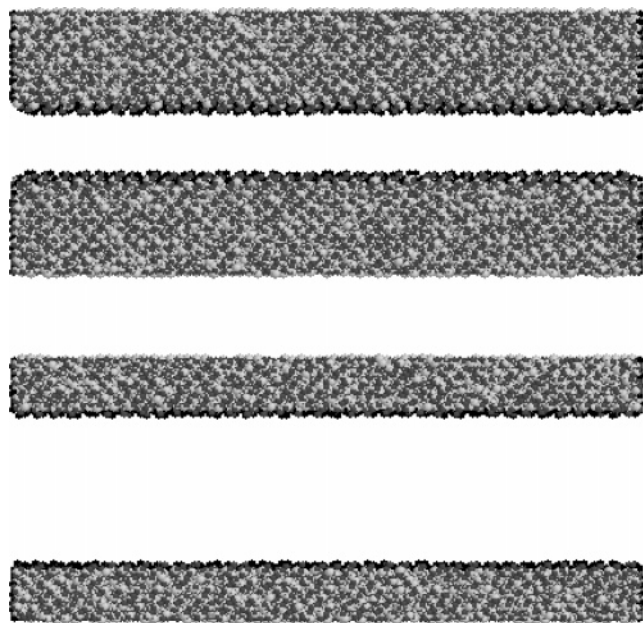*J. Phys. Chem. C, Vol. 111, No. 43, 2007* **15761**

Figure 1. Transversal views of MCM-41 silica nanopores having a regular cylindrical diameter $D = 3.2$ nm (pore A1, top) and $D = 6.4$ nm (pore A2, bottom). White and gray spheres are oxygen and silicon atoms, respectively. Black spheres correspond to hydrogen atoms, which delimit the pore surface.

chemical potential μ and temperature T.[31-33] The absolute adsorption isotherm is given by the ensemble average of the number of adsorbed atoms as a function of the pressure of the gas reservoir P (the latter is obtained from the chemical potential according to the bulk equation of state for an ideal gas). Interactions between the argon and the substrate atoms were calculated using the PN-TraZ potential as reported for rare gas adsorption in zeolite[34] or in porous silica glass.[20] The intermolecular energy is written as the sum of the dispersion interaction with a repulsive short-range contribution and an induction term due to the interaction of the adsorbed atom with the local field created by the partial charges of the atoms in the substrate. Values of the interaction parameters as well as details of the intermolecular potential functions can be found in the previous work by Pellenq and Levitz.[20] We calculated the adsorbate/ substrate interaction using an energy grid;[35] the potential energy is calculated at each corner of each elementary cube (about 1 Å^3). An accurate estimate of the energy is then obtained by a linear interpolation of the grid values. Such a procedure enables simulation of adsorption in mesoporous media of complex morphology and topologies without a direct summation over matrix species in the course of GCMC runs.[23,36-38] The argon/ argon interaction was calculated using a Lennard-Jones potential with $\epsilon_{Ar} = 120$ K and $\sigma_{Ar} = 0.34$ nm.[39] Both the saturation pressure of the solid and that of the supercooled liquid can be used to calculate the adsorption isotherm in reduced units as 77 K is below the triple point of argon. The saturation pressure P_0 used in the present work corresponds to that of the metastable liquid as given by the Kofke equation of state for Lennard-Jones fluids.[40] This choice is supported by previous DFT calculations by Neimark et al.[41] and molecular simulations by Coasne and Pellenq[23] in which it was found that confined argon after capillary condensation in silica pores at 77 K is liquid-like. A Monte Carlo step in the present work corresponds to a particle displacement attempt and either a deletion or a creation attempt. Deletion and creation were attempted in the entire volume of the simulation box. The system was first allowed to equilibrate in the course of a first GCMC run. Afterward, the
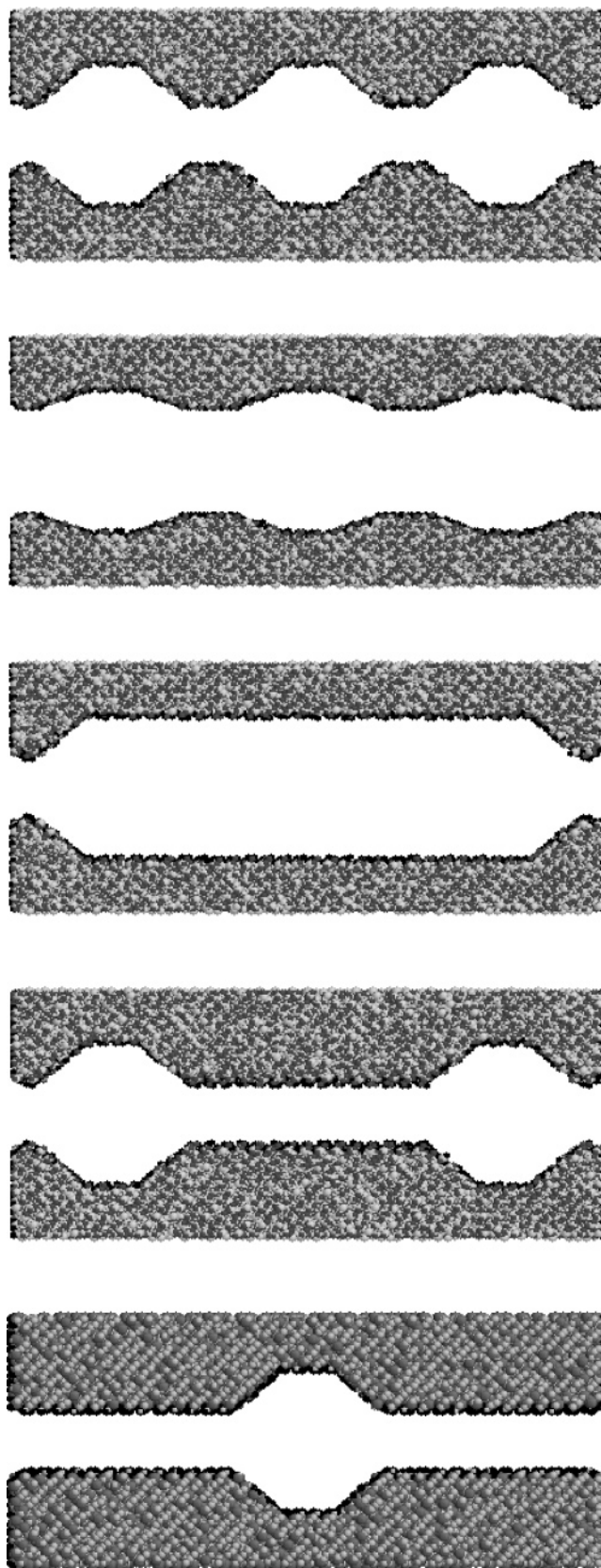

Figure 2. Transversal views of the MCM-41 silica nanopores having a constriction. From top to bottom: pore B1, pore B2, pore B3, pore B4, and pore B5 (see Table 1). White and gray spheres are oxygen and silicon atoms, respectively. Black spheres correspond to hydrogen atoms, which delimit the pore surface.

number of particles in the system and the isosteric heat of adsorption, which fluctuate about a steady value, were averaged using 10^5 Monte Carlo steps per particle. The uncertainty on
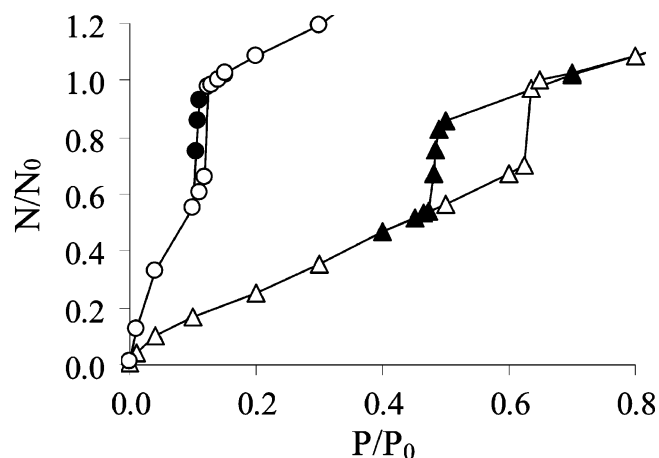
Figure 3. Ar adsorption isotherms at 77 K in a MCM-41 with $D = 3.2$ nm (circles, pore A1) and $D = 6.4$ nm (triangles, pore A2). Open and closed symbols correspond to the adsorption and desorption data, respectively. The adsorbed amounts have been normalized to the total number of adsorbed atoms, N_0, when the pores are completely filled (at the upper closure point of the capillary condensation hysteresis).

the adsorbed amounts and isosteric heat of adsorption is of a few percents (the latter corresponds to the statistical error on the set of data used to calculate the average values).

3. Results

3.1. Regular Cylindrical Pores. The argon adsorption isotherms obtained at 77 K for the regular cylindrical nanopores with $D = 3.2$ nm and $D = 6.4$ nm (pore A1 and pore A2) are shown in Figure 3. Adsorbed amounts have been normalized to the total number of atoms, N_0, when the pores are filled (at the upper closure point of the capillary condensation hysteresis). The argon adsorption isotherms for these two pores conform to the typical behavior observed in the experiments for adsorption/ condensation in cylindrical nanopores MCM-41;[1] the adsorbed amount increases continuously in the multilayer adsorption regime until a jump occurs because of the capillary condensation of the fluid within the pore. The condensation pressures are $P = 0.12$ P_0 for the nanopore with $D = 3.2$ nm and $P = 0.62$ P_0 for that with $D = 6.4$ nm. The evaporation pressures, $P = 0.11$

P_0 for $D = 3.2$ nm and $P = 0.49$ P_0 for $D = 6.4$ nm, are lower than the condensation pressures, so that hysteresis loops are observed. Figure 4 shows simulation snapshots of Ar atoms adsorbed in this pore at different pressures upon adsorption and desorption. Inspection of these snapshots shows that the surface of the regular silica nanopore is covered by a molecularly homogeneous thick cylindrical film at the onset of capillary condensation. As expected for a regular nanopore, condensation occurs through an irreversible discontinuous transition between the partially filled and the completely filled configurations. We found in agreement with previous works on adsorption/desorption in cylindrical pores[38,42] that the evaporation for pores of a finite length occurs through the displacement at equilibrium of a hemispherical meniscus along the pore axis (Figure 4). This result departs from what is observed for pores having an infinite length; the evaporation occurs necessarily through cavitation as there is no interface between the confined liquid and the external gas phase.[23,42–49] The configuration shown in the lower right part of Figure 4 is stable over the length of the second simulation run performed after equilibration of the system (for details, see section 2.2). As noted above, desorption for opened cylindrical pores occurs at equilibrium and proceeds through a continuous series of such configurations where the hemispherical meniscus is receding along the pore axis (the configuration shown in the lower right part of Figure 4 is simply an example of one of these configurations). The nature and transition pressures of the adsorption and desorption processes are summarized in Tables 2 and 3 for the different pores considered in this work. The hysteresis loop for the pore with $D = 6.4$ nm is much larger than that for the pore with $D = 3.2$ nm. This result can be explained as follows. We know from previous experimental,[50–53] theoretical,[54–57] and molecular simulation[38,58,59] works that there is a temperature, the so-called capillary condensation temperature T_{cc}, above which capillary condensation in nanoporous solids becomes reversible and continuous. This pseudocritical temperature corresponds to the threshold of reversible capillary condensation of the confined fluid. As the temperature approaches T_{cc} the hysteresis loop shrinks and, finally, disappears for $T = T_{cc}$. We also know that T_{cc} increases as the pore diameter increases. Consequently, for a given temperature T, the hysteresis loop for the small pore
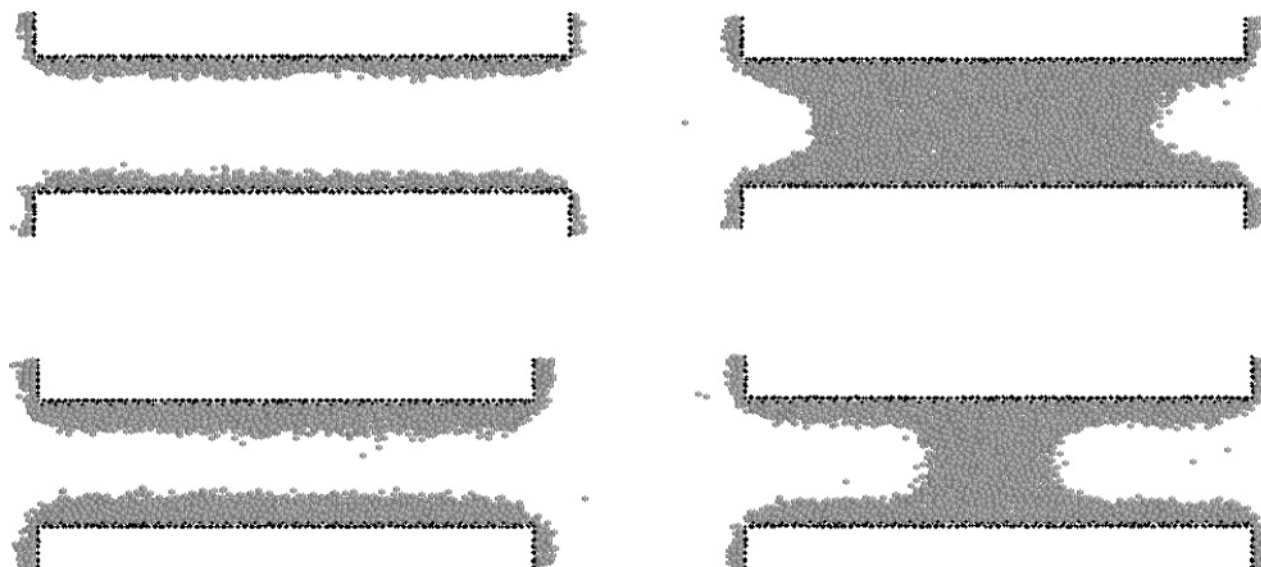

Figure 4. Configurations of argon atoms adsorbed at 77 K in a regular cylindrical silica pore of a diameter $D = 6.4$ nm (pore A1). (Left) Adsorption: $P = 0.30$ P_0 (top) and $P = 0.62$ P_0 (bottom). (Right) Desorption: $P = 0.49$ P_0 (top) and $P = 0.48$ P_0 (bottom). Black spheres correspond to the hydrogen atoms, which delimit the pore surface, and the light colored spheres are Ar atoms.

TABLE 2: Condensation and Evaporation Pressures for the Different Silica Nanopores Considered in This Work[a]

porous material	adsorption	desorption
	Regular Pores	
pore A1	$P = 0.12\ P_0$	$P = 0.11\ P_0$
pore A2	$P = 0.62\ P_0$	$P = 0.49\ P_0$
	Constricted Pores	
pore B1	constrictions, $P = 0.22\ P_0$ cavities, $P = 0.42\ P_0$	constrictions and cavities near the pore openings, $P = 0.21\ P_0$ constrictions and cavities in the pore center, $P = 0.12\ P_0$
pore B2	constrictions and cavities, $P = 0.52\ P_0$	constrictions and cavities near the pore openings, $P = 0.38\ P_0$ constrictions and cavities in the pore center, $P = 0.32\ P_0$
pore B3	constrictions, $P = 0.38\ P_0$ cavities, $P = 0.50\ P_0$	$P = 0.20\ P_0$
pore B4	constriction in the pore center, $P = 0.11\ P_0$ constrictions and cavities 　near the pore openings, $P = 0.42\ P_0$	constrictions and cavities near the pore openings, $P = 0.21\ P_0$ constriction in the pore center, $P = 0.11\ P_0$
pore B5	constrictions, $P = 0.13\ P_0$ cavity, $P = 0.42\ P_0$	cavity, $P = 0.13\ P_0$ constrictions, $P = 0.11\ P_0$

[a] Note that the filling and emptying pressures reported in the table correspond to the pressure at the onset of condensation and evaporation, respectively. The associated transition is in fact located between that pressure and the nearest one (above in the case of adsorption and below in the case of desorption).

TABLE 3: Nature of the Adsorption and Desorption Processes for the Different Silica Nanopores Considered in This Work[a]

porous material	adsorption	desorption
	Regular Pores	
pore A1	metastable	equilibrium
pore A2	metastable	equilibrium
	Constricted Pores	
pore B1	quasi-equilibrium constrictions, equilibrium cavities, metastable	metastable (pore blocking) constrictions and cavities near the pore openings, metastable constrictions and cavities in the pore center, metastable
pore B2	metastable constrictions and cavities, metastable	metastable (pore blocking) constrictions and cavities near the pore openings, metastable constrictions and cavities in the pore center, metastable
pore B3	quasi-equilibrium constrictions, equilibrium cavities, metastable	metastable (pore blocking)
pore B4	quasi-equilibrium constriction in the pore center, metastable constrictions and cavities near 　the pore openings, metastable	quasi-equilibrium constrictions and cavities near the pore openings, metastable constriction in the pore center, equilibrium
pore B5	quasi-equilibrium constrictions, metastable cavity, metastable	quasi-equilibrium constrictions, equilibrium cavity, cavitation

[a] Quasi-equilibrium is used when the path is made of both at equilibrium (continuous, reversible) and metastable (discontinuous, irreversible) parts.

($D = 3.2$ nm) must be smaller than that for the large pore ($D = 6.4$ nm) as T is closer to T_{cc} for the small pore than that for the large pore. We note that the adsorption isotherms for the two regular cylindrical pores conform to the experimental behavior observed for MCM-41 samples. This suggests that these materials are made up of cylindrical pores having no or only very smooth morphological defects.

3.2. Cylindrical Pores with Constrictions. We discuss in this subsection the results obtained for the four cylindrical pores having constrictions (see Table 1). As for the regular nanopores, the results for the constricted pores (nature and transition pressures) are summarized in Tables 2 and 3. We note that recent DFT calculations,[60] MC simulations[20,44,61−64] and experiments[65,66] of adsorption and desorption in constricted pores and disordered porous materials have been reported in the literature. The argon adsorption isotherm at 77 K for the silica nanopore of a diameter $D = 6.4$ nm and a constriction with $D_c = 3.2$ nm (pore B1) is shown in Figure 5. Adsorbed amounts have been normalized to the total number of atoms, N_0, when the pore is filled (at the upper closure point of the capillary condensation hysteresis). We also present in Figure 6 a series of configurations
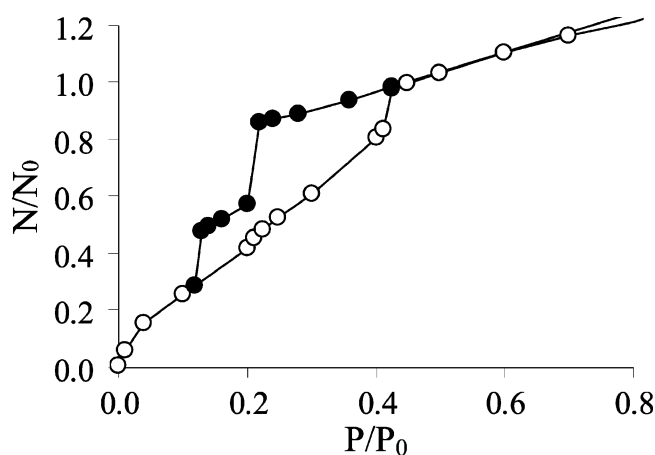

Figure 5. Ar adsorption isotherm at 77 K in a silica pore of a diameter $D = 6.4$ nm and a constriction $D_c = 3.2$ nm (pore B1). Open and closed symbols correspond to the adsorption and desorption data, respectively. The adsorbed amounts have been normalized to the total number of adsorbed atoms when the pores are completely filled, N_0 (at the upper closure point of the capillary condensation hysteresis).
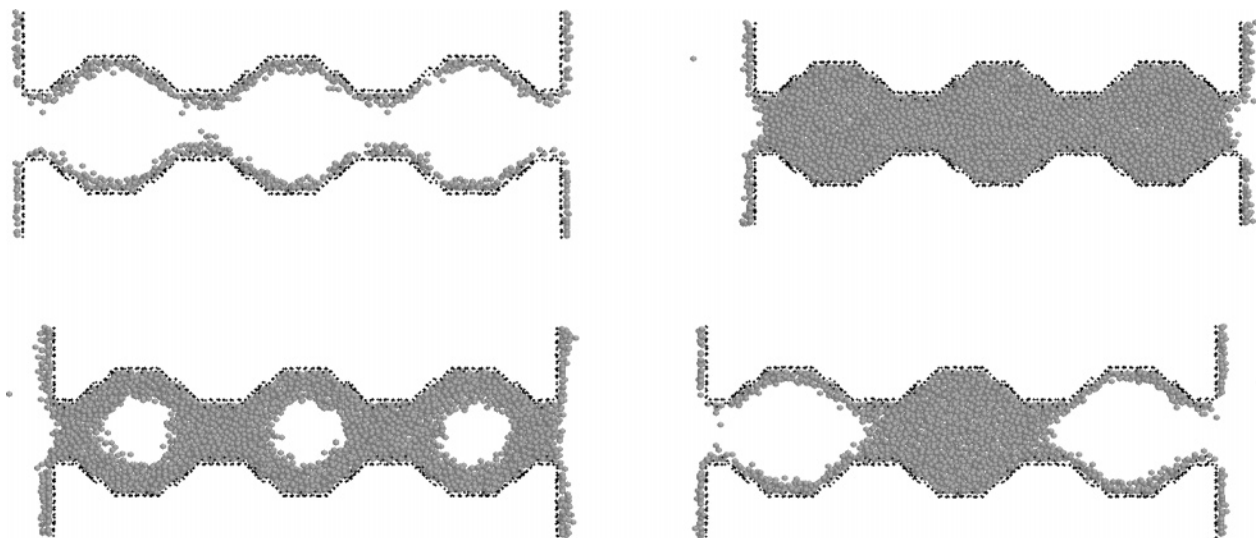
Figure 6. Configurations of argon atoms adsorbed at 77 K in a silica pore of a diameter $D = 6.4$ nm and a constriction $D_c = 3.2$ nm (pore B1). (Left) Adsorption: $P = 0.10\,P_0$ (top) and $P = 0.40\,P_0$ (bottom). (Right) Desorption: $P = 0.24\,P_0$ (top) and $P = 0.14\,P_0$ (bottom). Black spheres correspond to the hydrogen atoms, which delimit the pore surface, and the light colored spheres are Ar atoms.
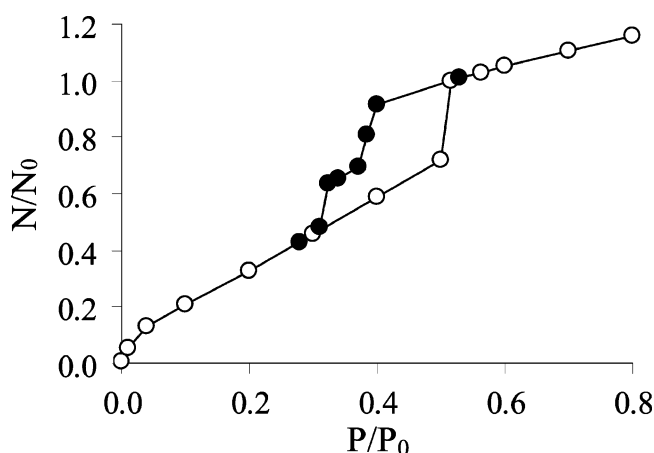

Figure 7. Ar adsorption isotherm at 77 K in a silica pore of a diameter $D = 6.4$ nm and a constriction $D_c = 4.8$ nm (pore B2). Open and closed symbols correspond to the adsorption and desorption data, respectively. The adsorbed amounts have been normalized to the total number of adsorbed atoms when the pores are completely filled, N_0 (at the upper closure point of the capillary condensation hysteresis).

of Ar atoms adsorbed in this pore at different pressures upon adsorption and desorption. At low pressures, the pore surface is covered by a quasihomogeneous layer of Ar atoms (see Figure 6). The filling of the pore starts at $P \sim 0.22\,P_0$ with the continuous condensation of Ar atoms in the constrictions with $D = 3.2$ nm. This condensation pressure is larger than that obtained for the cylindrical pore with $D = 3.2$ nm. This result is due to the fact that the constriction has a smaller length than the regular cylindrical pore; as a result, the fluid within the constriction is less stable as it interacts with less wall atoms than in the regular cylindrical pore. This result is consistent with previous molecular simulation works[42,49] which have shown that the condensation pressure in a pore of an infinite length is smaller than that in a pore of a finite length. Condensation in the constrictions leads to the presence of hemispherical menisci in the interfacial region between the large cavities with $D = 6.4$ nm and the constrictions with $D = 3.2$ nm. As shown in Figure 6 (second snapshot), these curved interfaces together with the film adsorbed on the pore wall define gas nanobubbles inside the large cavities. As the pressure increases, we observe the displacement at equilibrium (reversible and continuous) of these

menisci toward the center of the cavities with $D = 6.4$ nm; that is, the radius of the gas bubbles located inside the cavities diminishes. Finally, the pore gets completely filled once the irreversible condensation of the gas nanobubbles occurs at a pressure $P = 0.42\,P_0$. We note that the condensation of the gas bubbles is a metastable transition located at a pressure higher than the equilibrium pressure (for a detailed discussion, see ref 23). Thus, the different parts of the filling mechanism are either at equilibrium (continuous condensation in the constrictions, displacement of the hemispherical menisci) or metastable (gas bubble). The condensation pressure for the gas nanobubbles in the cavities with $D = 6.4$ nm is lower than that for the regular cylindrical pore having the same diameter because it consists of the filling of a spherical cavity. A theoretical expression of the condensation pressure for a gas bubble can be obtained by introducing in the Kelvin equation the corresponding form factor; the logarithm of the metastable condensation pressure in a spherical cavity $\ln(P_c/P_0)_{sphere}$ should be twice that for a cylindrical cavity $\ln(P_c/P_0)_{cylinder}$.

Because of the different condensation pressures for the constriction with $D = 3.2$ nm and cavity with $D = 6.4$ nm, the adsorption branch for this pore appears much smoother (nonvertical) than that observed for the regular pores with $D = 3.2$ nm and $D = 6.4$ nm. Malanoski and Van Swol have obtained a similar result for square ink-bottled pores.[67] From a fundamental viewpoint, the effect of the constriction is to attenuate the jump in adsorbed amount, which reveals the capillary condensation phenomenon. Kierlik et al. [68−70] have shown by lattice gas calculations that the attenuation of the jump in the adsorbed amounts accompanying the condensation phenomenon is expected in the case of porous media with interconnected pores (topological disorder) of a complex geometry (morphological disorder). This effect has been also observed in experiment[71] or simulation[20,72,73] for disordered porous matrices such as Vycor. A decrease of the discontinuity in adsorbed amounts has also been obtained in adsorption experiments by Van der Voort et al.[47] who have prepared silica cylindrical pores (SBA-15) with and without constrictions. These authors have found that the nitrogen adsorption isotherm (77 K) for the constricted pores has a much smoother adsorption branch than that for regular cylindrical pores.
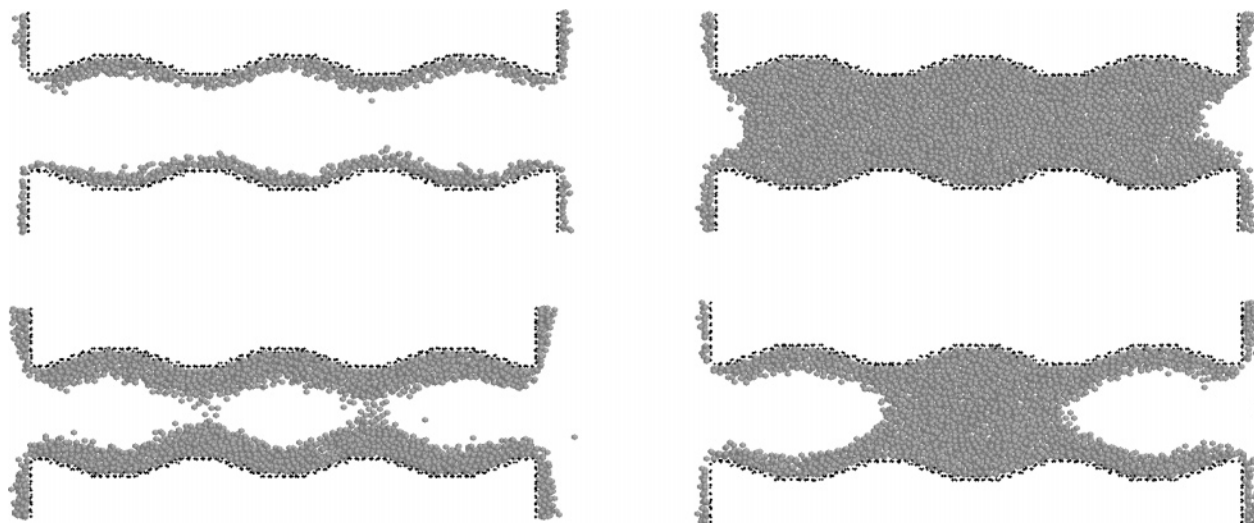
Gas Adsorption in Nanoporous Silicas

J. Phys. Chem. C, Vol. 111, No. 43, 2007 **15765**

Figure 8. Configurations of argon atoms adsorbed at 77 K in a silica pore of a diameter $D = 6.4$ nm and a constriction $D_c = 4.8$ nm (pore B2). (Left) Adsorption: $P = 0.20\ P_0$ (top) and $P = 0.52\ P_0$ (bottom). (Right) Desorption: $P = 0.40\ P_0$ (top) and $P = 0.34\ P_0$ (bottom). Black spheres correspond to the hydrogen atoms, which delimit the pore surface and the light colored spheres are Ar atoms.

Starting with the completely filled pore (Figure 6), the desorption branch for the constricted pore (pore B1) is a two-step process (Figure 5). As the pressure is decreased, we first observe at $P = 0.21\ P_0$ the desorption of Ar atoms confined in the two pore constrictions near the pore openings toward the external bulk reservoirs. Such a desorption triggers the evaporation at the same pressure of the fluid confined in the two cavities with $D = 6.4$ nm located near the pore external surfaces. In contrast, the cavity with $D = 6.4$ nm and constrictions with $D = 3.2$ nm located in the pore center remain filled by the liquid at this pressure (see Figure 6, snapshot 4). This result can be explained by the fact that the fluid confined in the pore center (constrictions or cavities) is more stable than that near the pore surface as it interacts with a larger number of wall atoms. Finally, the desorption mechanism for this pore ends with the evaporation at $P = 0.12\ P_0$ of Ar atoms in the pore center, that is, the two constrictions with $D = 3.2$ nm and the cavity with $D = 6.4$ nm. Such a complex desorption process can be described as a double pore blocking mechanism as both the desorption of the large cavities (in the pore center and near the pore openings) are triggered by the evaporation of the constrictions that isolate them from the gas phase. This result shows that the pore external surfaces introduce some heterogeneity in the overall desorption process (in the sense that the desorption pressure of the fluid near the pore opening is different from that of the fluid in the pore center).

The argon adsorption isotherm at 77 K for the silica nanopore of a diameter $D = 6.4$ nm and a constriction with $D_c = 4.8$ nm (pore B2) is shown in Figure 7. We also present in Figure 8a series of configurations of Ar atoms adsorbed in this pore at different pressures upon adsorption and desorption. Again, the pore surface is covered by a quasihomogeneous layer of Ar atoms at low pressures (see Figure 8). The filling of the pore occurs at $P = 0.52\ P_0$ with the irreversible and discontinuous condensation in both the constrictions with $D = 4.8$ nm and the cavities with $D = 6.4$ nm. This adsorption mechanism departs from that for the previous constricted pore (pore B1) for which the constrictions fill at a pressure smaller than that for the large cavities. This result is due to the fact that the size difference for the pore B2 is not large enough to observe different condensation pressures. For characterization purposes, this result shows that a steep condensation branch can be observed even though the pore exhibits some undulations along
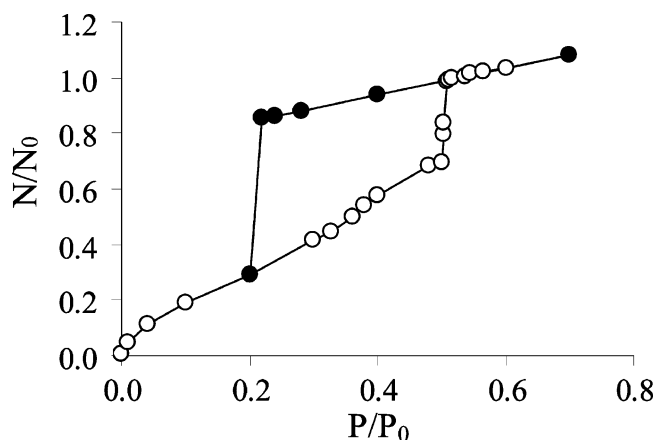

Figure 9. Ar adsorption isotherm at 77 K in a silica pore of a diameter $D = 6.4$ nm, a length $L = 23.4$ nm, and a constriction $D_c = 3.2$ nm (pore B3). Open and closed symbols correspond to the adsorption and desorption data, respectively. The adsorbed amounts have been normalized to the total number of adsorbed atoms when the pores are completely filled, N_0 (at the upper closure point of the capillary condensation hysteresis).

its axis (provided that the diameter of such undulations is close to that of the large cavities). The unique condensation pressure in the cavities with $D = 6.4$ nm and constrictions with $D = 4.8$ nm for this undulating pore is lower than that for the regular cylindrical pore having the same diameter because it consists of the filling of a noncylindrical cavity; the curvature radius for such cavities is larger than that for a regular cylindrical pore so that the condensation pressure is lowerered (see snapshot in Figure 7).

As for the previous constricted pore (pore B1), the desorption branch for pore B2 consists of a double pore blocking mechanism (Figure 7). Starting with the completely filled pore (Figure 8), we first observe at $P = 0.38\ P_0$ the desorption of the two pore constrictions near the pore openings, which provokes the evaporation of the two cavities with $D = 6.4$ nm located near the pore external surfaces. At this pressure, the cavity with $D = 6.4$ nm and the constrictions with $D = 4.8$ nm in the pore center remain filled by the liquid (see Figure 8, snapshot 4). Again, this result can be explained by the fact that the fluid confined in the pore center (constrictions or cavities) is more stable than that near the pore surface as it interacts with a larger
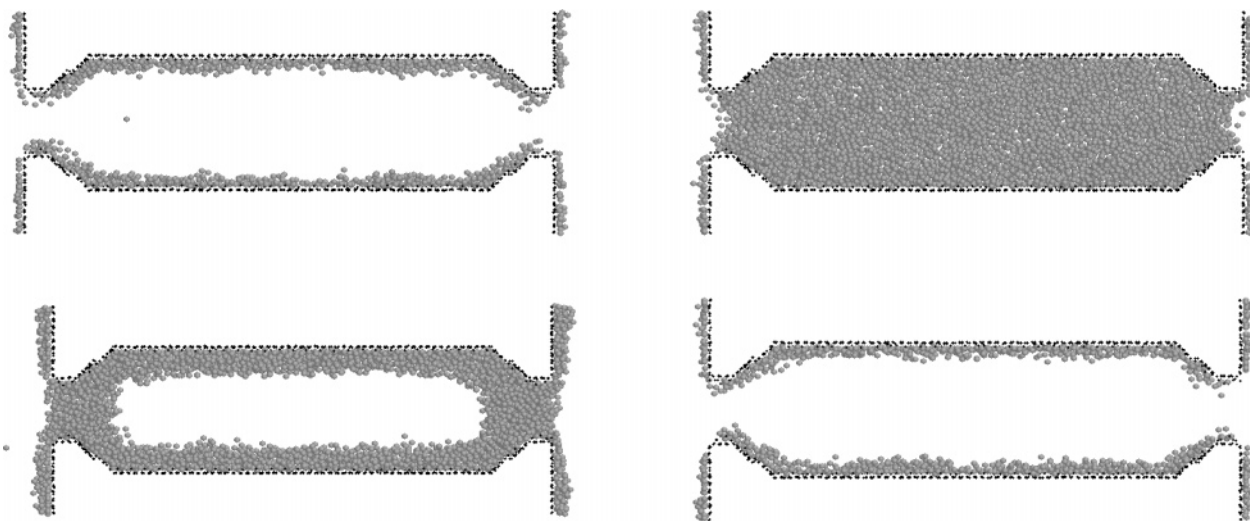
Figure 10. Configurations of argon atoms adsorbed at 77 K in a silica pore of a diameter $D = 6.4$ nm, a length $L = 23.4$ nm, and a constriction $D_c = 3.2$ nm (pore B3). (Left) Adsorption: $P = 0.20\ P_0$ (top) and $P = 0.50\ P_0$ (bottom). (Right) Desorption: $P = 0.22\ P_0$ (top) and $P = 0.20\ P_0$ (bottom). Black spheres correspond to the hydrogen atoms, which delimit the pore surface, and the light colored spheres are Ar atoms.

number of wall atoms. Finally, the desorption mechanism for this pore ends with the evaporation at $P = 0.32\ P_0$ of Ar atoms in the pore center, that is, the two constrictions with $D = 3.2$ nm and the cavity with $D = 6.4$ nm in the pore center. Again, such a complex desorption process can be described as a double pore blocking mechanism as both the desorption of the large cavities (in the pore center and near the pore openings) are triggered by the evaporation of the constrictions that isolate them from the gas phase.

The argon adsorption isotherm at 77 K for the silica nanopore consisting of a long cavity of a diameter $D = 6.4$ nm and a length $L = 23.4$ nm and a constriction with $D_c = 3.2$ nm (pore B3) is shown in Figure 9. We also present in Figure 10 configurations of Ar atoms in this pore at different pressures upon adsorption and desorption. Starting with the low pressure configurations where the pore surface is covered by a homogeneous layer of Ar atoms, the filling of the pore occurs at $P = 0.38\ P_0$ with the reversible continuous condensation in the two constrictions with $D = 3.2$ nm. Condensation in the constrictions leads to the presence of hemispherical menisci in the interfacial region between the cavity with $D = 6.4$ nm and the constrictions with $D = 3.2$ nm. These curved interfaces together with the film adsorbed on the pore wall define a gas nanobubble having the shape of an ellipsoid (Figure 10). As the pressure increases, we observe the growth at equilibrium (reversible and continuous) of the film adsorbed at the pore surface. Finally, the pore gets completely filled at $P = 0.50\ P_0$ with the irreversible condensation of the gas nanobubble. Such a condensation is a two-step process that occurs in a very limited pressure range. First, we observe the reversible deformation of the nanobubble that tends to adopt a more symmetrical shape. Once the nanobubble is of a spherical shape, its irreversible condensation occurs within the cavity. Again, the condensation of the gas bubble is a metastable transition located at a pressure higher than the equilibrium pressure. The condensation pressure for the gas nanobubbles in the cavities with $D = 6.4$ nm is lower than that for the regular cylindrical pore having the same diameter because it consists of the filling of a spherical cavity. The desorption for this pore having a long cavity (pore B3) occurs through a simple pore blocking mechanism. Starting with the completely filled pore (Figure 10), the evaporation of the cavity with $D = 6.4$ nm is triggered by the evaporation of the two constrictions with $D = 3.2$ nm near the pore openings. This
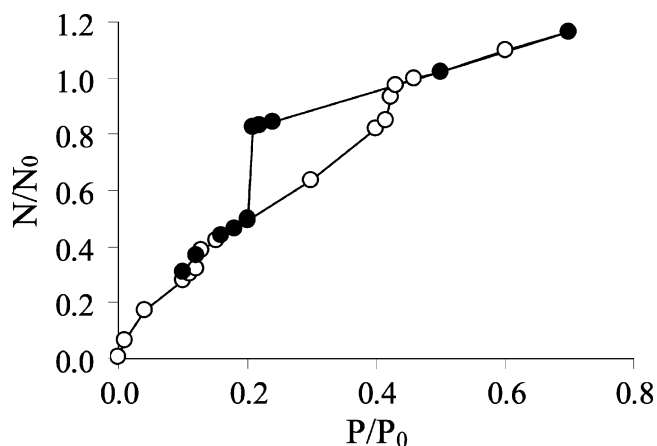

Figure 11. Ar adsorption isotherm at 77 K in a silica pore of a diameter $D = 6.4$ nm and a constriction $D_c = 3.2$ nm of a length $L_c = 10.7$ nm (pore B4). Open and closed symbols correspond to the adsorption and desorption data, respectively. The adsorbed amounts have been normalized to the total number of adsorbed atoms when the pores are completely filled, N_0 (at the upper closure point of the capillary condensation hysteresis).

desorption process departs from the double pore blocking mechanism that is observed for the first two constricted pores (pores B1 and B2).

The argon adsorption isotherm at 77 K for the silica nanopore with a cavity of a diameter $D = 6.4$ nm and a constriction of a diameter $D_c = 3.2$ nm and a length $L = 10.7$ nm (pore B4) is shown in Figure 11. We also present in Figure 12 some configurations of Ar atoms adsorbed in this pore at different pressures upon adsorption and desorption. Again, the pore surface is covered by a quasihomogeneous layer of Ar atoms at low pressures (Figure 12). As the pressure increases, the reversible and continuous filling of the long constriction with $D = 3.2$ nm occurs at $P = 0.11\ P_0$. Interestingly, the condensation pressure for this long constriction is lower than that for a constriction having the same diameter but a shorter length; the condensation pressure for the constriction with $D = 3.2$ nm and $L = 2.1$ nm is $P = 0.22\ P_0$ (see the results for pore B1). This result shows that the confined liquid is less stable as the constriction becomes shorter because it interacts with less wall atoms. This result also indicates that we are in a range of cavity or constriction sizes (length, diameter, etc.) for which
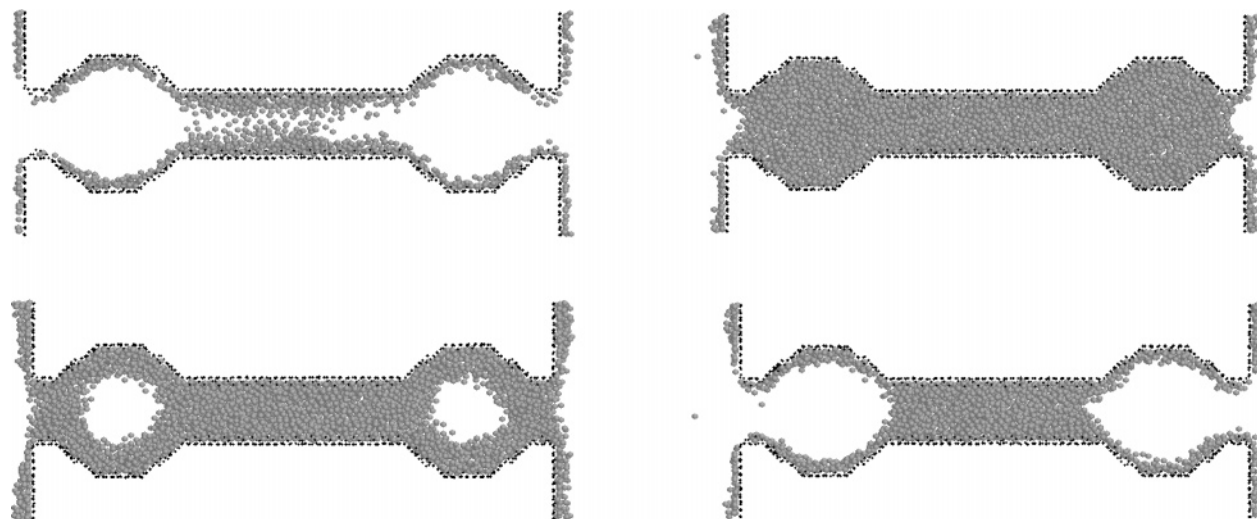
Gas Adsorption in Nanoporous Silicas

J. Phys. Chem. C, Vol. 111, No. 43, 2007 **15767**

Figure 12. Configurations of argon atoms adsorbed at 77 K in a silica pore of a diameter $D = 6.4$ nm and a constriction $D_c = 3.2$ nm of a length $L_c = 10.7$ nm (pore B4). (Left) Adsorption: $P = 0.12\ P_0$ (top) and $P = 0.42\ P_0$ (bottom). (Right) Desorption: $P = 0.21\ P_0$ (top) and $P = 0.16\ P_0$ (bottom). Black spheres correspond to the hydrogen atoms, which delimit the pore surface and the light colored spheres are Ar atoms.

the condensation pressure depends on the pore length. The filling mechanism for this pore (pore B4) ends with the condensation at $P = 0.42\ P_0$ in the two cavities with $D = 6.4$ nm near the pore surface. We found the same condensation pressure for such cavities when they are located between shorter constrictions (pore B1). This result suggests that the condensation pressure for the largest cavity is not very sensitive to the length of the constrictions that isolate it from the gas phase. This departs from the evaporation mechanism, which is found to be very dependent on the morphological properties of the constrictions. The desorption for this pore having a long constriction occurs through a two-step process. First, we observe at $P = 0.21\ P_0$ the desorption of the two cavities with $D = 6.4$ nm through a simple pore blocking mechanism. Starting with the completely filled pore (Figure 12), the evaporation of the cavities is triggered by the desorption of the two constrictions with $D = 3.2$ nm near the pore openings. Of course, this evaporation pressure corresponding to that of the constrictions near the pore openings ($L = 1.1$ nm) is the same as that found for the pores having such constrictions (i.e., pores B1 and B3). Once the two cavities are emptied, we observe at $P = 0.11\ P_0$ the evaporation at equilibrium of the long constriction that occurs through the displacement at equilibrium of a hemispherical meniscus along the pore axis.

The argon adsorption isotherm at 77 K for the silica nanopore with a cavity of a diameter $D = 6.4$ nm, isolated from the bulk external phase by two constrictions of a diameter $D_c = 3.2$ nm and a length $L = 9.6$ nm (pore B5) is shown in Figure 13. We also present in Figure 14 some configurations of Ar atoms adsorbed in this pore at different pressures upon adsorption and desorption. Again, the pore surface is covered by a quasihomogeneous layer of Ar atoms at low pressures (Figure 14). As the pressure increases, the filling of the long constriction with $D = 3.2$ nm occurs at $P = 0.13\ P_0$. This condensation pressure is very close to that of the constriction in the adsorption isotherm for the pore B4 (having also a long constriction with $D = 3.2$ nm and $L = 10.7$ nm). The filling mechanism for this pore (pore B5) ends with the condensation at $P = 0.42\ P_0$ in the cavity with $D = 6.4$ nm. Again, the same condensation pressure was found for such cavities when they are located between shorter constrictions (pore B1), which suggests that the condensation pressure for the largest cavity is not very sensitive to the length of the constrictions that isolate it from the gas phase. The
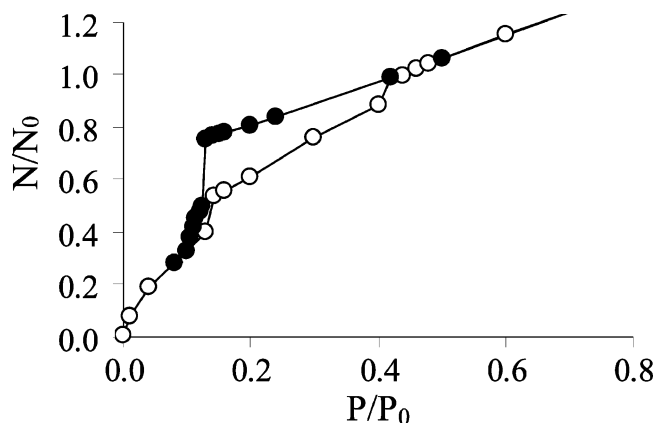

Figure 13. Ar adsorption isotherm at 77 K in a silica pore of a diameter $D = 6.4$ nm and a constriction $D_c = 3.2$ nm of a length $L_c = 9.6$ nm (pore B5). Open and closed symbols correspond to the adsorption and desorption data, respectively. The adsorbed amounts have been normalized to the total number of adsorbed atoms when the pores are completely filled, N_0 (at the upper closure point of the capillary condensation hysteresis).

desorption for this pore having a long constriction starts at $P = 0.13\ P_0$ through cavitation; that is, the large cavity with $D = 6.4$ nm empties through the spontaneous nucleation of a gas bubble while the constrictions with $D = 3.2$ nm remain filled by the liquid (Figure 14). Once the cavity with $D = 6.4$ nm is empty, we observe at $P = 0.11\ P_0$ the evaporation at equilibrium of the long constriction that occurs through the displacement at equilibrium of a hemispherical meniscus along the pore axis. As expected, this evaporation pressure is identical to that for the long constriction of the same diameter in pore B4.

The isosteric heat Q_{st} of adsorption for argon at 77 K in the different silica nanopores is shown in Figure 15. Data are reported as a function of the adsorbed amount normalized to the total number of atoms, N_0, when the pores are filled (at the upper closure point of the capillary condensation hysteresis). For all pores, Q_{st} has been calculated from the fluctuations over the number of particles and energy in the course of the simulations. The Q_{st} curves for all pores are very similar over the entire scale of adsorbed amounts (this set of curves seem to fall on the same master curve). We note that the Q_{st} data for $N \sim N_0$ show some deviation as a result of the poor statistics in the high loading range due to the small fluctuations in the
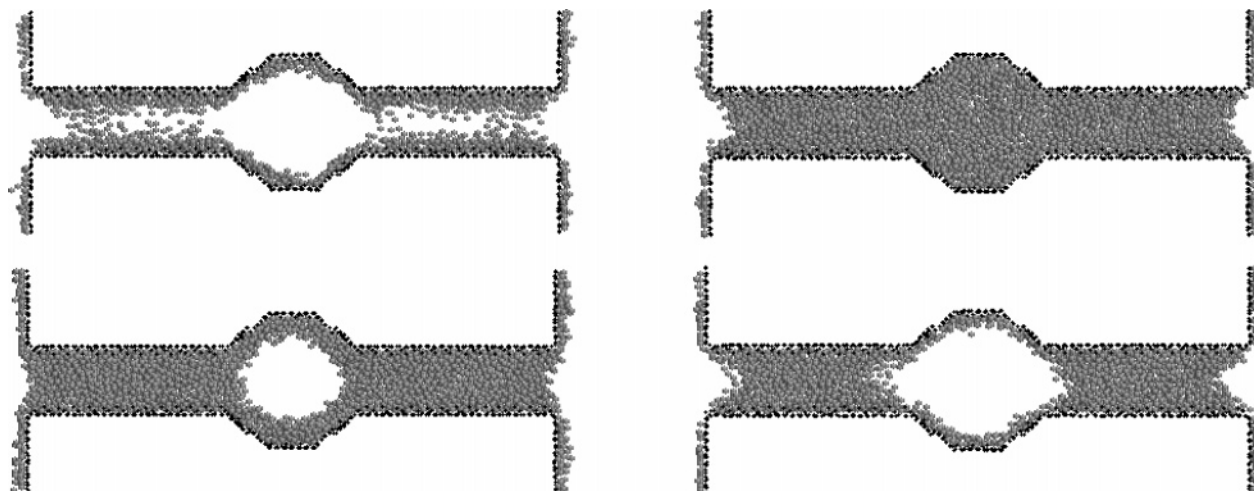
Figure 14. Configurations of argon atoms adsorbed at 77 K in a silica pore of a diameter $D = 6.4$ nm and a constriction $D_c = 3.2$ nm of a length $L_c = 9.6$ nm (pore B4). (Left) Adsorption: $P = 0.13\ P_0$ (top) and $P = 0.30\ P_0$ (bottom). (Right) Desorption: $P = 0.13\ P_0$ (top) and $P = 0.12\ P_0$ (bottom). Black spheres correspond to the hydrogen atoms, which delimit the pore surface and the light colored spheres are Ar atoms.
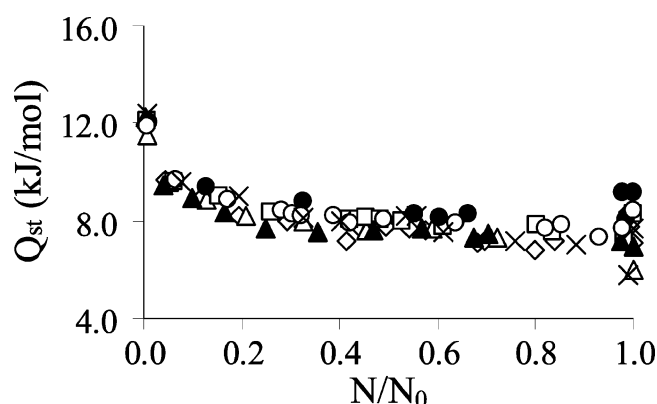

Figure 15. Isosteric heat of adsorption of Ar at 77 K in various MCM-41 pores. Closed symbols are for regular cylindrical pores with $D = 3.2$ nm (circles, pore A1) and $D = 6.4$ nm (triangles, pore A2). Open symbols and crosses are for pores having a constriction: (squares) pore B1, (triangles) pore B2, (diamonds) pore B3, (circles) pore B4, (crosses) pore B5.

number of particles when the pores are filled. The value of the isosteric heat at very low coverage, $Q_{st}(0) = 12.0$ kJ/mol, is in good agreement with that observed in the experiments (11.0 kJ/mol).[41] As the pressure increases, the isosteric heat decreases until it reaches the heat of liquefaction of Ar at 77 K ($\sim 7-8$ kJ/mol). The fact that all of the Q_{st} data fall on the same curve suggests that microcalorimetry experiments and any measurement used to determine the energetics of adsorption in porous materials cannot be used to assess and characterize morphological defects such as constrictions, and so forth.

4. Discussion

In this paper, we report molecular simulations of adsorption of argon confined in silica nanopores without or with morphological defects (constrictions). From a fundamental point of view, these morphological defects are equivalent to chemical heterogeneity along the pore axis in the sense that they introduce some dispersion in the potential energy along the pore surface (see refs 74−79 for a detailed discussion on adsorption in chemically heterogeneous nanopores). All of the pores considered in this work are of a finite length and are connected to bulk reservoirs so that they mimic real materials for which the confined fluid is always in contact with the external gas phase (this departs from infinitely long pores for which the evaporation

of the confined liquid necessarily occurs through cavitation as there is no interface with the external phase). For the pores without constrictions, we considered two pore diameters, $D = 3.2$ nm and $D = 6.4$ nm, in order to address the effect of the pore size. For pores with constrictions, we address the effect of the size of these constrictions by varying their length and diameter. We also consider the effect of the number of constrictions. All of our results in terms of nature and transition pressures for the evaporation and condensation mechanisms are reported in Tables 2 and 3.

For all constricted pores, the pore surface is covered upon adsorption by a quasihomogeneous layer of Ar atoms at low pressures. As the pressure increases, the filling starts with the continuous condensation in the constrictions. The condensation pressure for such a filling mechanism increases with decreasing the length, increasing the size of the constriction, or both; the confined liquid becomes less stable as the constriction becomes shorter and wider because it interacts with less wall atoms. Because of the condensation in the constrictions, there are some curved interfaces (meniscus) in the region between the cavities that are empty and the constrictions that are filled with the liquid. In other words, there are in the large cavities some gas nanobubbles that are trapped between the confined liquid located in the constrictions. The pore filling ends with the deformation at equilibrium and the irreversible and discontinuous condensation of such gas nanobubbles (we found that the bubbles have a spherical shape when condensation occurs). This final condensation is a metastable transition located at a pressure higher than the equilibrium pressure. In addition, the transition pressure in these cavities is found to be lower than that for a regular cylindrical pore having the same diameter because it consists of the filling of a spherical cavity (i.e., the curvature radius is larger so that the confinement effect is stronger). Our results for the different constricted pores suggest that the condensation pressure for the large cavity depends on the diameter of the neighboring constrictions but not on their length.

The evaporation mechanism in the constricted pores is also found to depend on the size, length, and number of constrictions in the pores. The desorption can occur through a simple pore blocking effect; that is, the cavities empty when the constrictions that isolate them from the external bulk phase empty (pore B3). In some cases (pores B1 and B2), another evaporation process consisting of a "double pore blocking mechanism" is observed; both the evaporation of the region near the pore openings and

Gas Adsorption in Nanoporous Silicas

J. Phys. Chem. C, Vol. 111, No. 43, 2007 **15769**

that in the pore center are triggered through a pore blocking mechanism but occur at different pressures. We also identified a third mechanism (pore B4) that consists of a single pore blocking mechanism for the cavities located near the pore openings, followed by the evaporation at equilibrium of the constriction in the pore center (this second part of the mechanism is possible as the fluid confined in this constriction is in contact with the gas phase located in the large cavities). The fourth evaporation mechanism observed in the present work (pore B5) is the so-called cavitation phenomenon that has been reported in several studies.[44,48,61,65] Cavitation is an evaporation process that consists of the nucleation of a gas bubble within the pore while the constrictions remain filled by the liquid. The observation of pore blocking or cavitation depends on the relative stability of the liquid confined in the constriction and that confined in the cavity. Starting with a completely filled pore, the liquid trapped in a cavity isolated from the gas phase through a filled constriction experiences a depression as the pressure decreases. Pore blocking is observed if the liquid in the cavity can resist such a depression until the liquid in the constriction evaporates. In that case, the desorption of the liquid located in the constriction spontaneously triggers the evaporation of the liquid cavity (the latter being already at a pressure below its equilibrium pressure). On the other hand, cavitation is observed if the liquid in the cavity cannot resist the depression until the liquid in the constriction evaporates. In that case, the desorption of the liquid located in the constriction occurs through the spontaneous nucleation of a gas bubble, although the constriction remains filled by the liquid. The fact that we mainly observed in the present work evaporation through pore blocking (pore B1, B2, B3, and B4) can be explained as follows. For these four constricted pores considered, the large cavities are isolated from the gas reservoir through short constrictions. The liquid confined in such constrictions is not very stable as it does not interact with a large number of atoms from the silica substrate. As a result, the evaporation of the cavities for such systems is rather controlled through pore blocking effects. This interpretation is corroborated by the fact that cavitation is observed in the case of pore B5 for which the cavity is isolated from the bulk external phase by long constrictions.

5. Conclusion

Our findings can be summarized as follows. The adsorption isotherms for the regular cylindrical pores conform to the typical experimental behavior for MCM-41 as the adsorbed amount increases continuously in the multilayer adsorption regime until a jump occurs because of capillary condensation of the fluid within the pore. The evaporation pressures are lower than the condensation pressures, so that hysteresis loops are observed. As expected for a regular nanopore, condensation occurs through an irreversible and discontinuous transition between the partially filled and the completely filled configurations. The condensation and evaporation mechanisms for the pores with constrictions depart significantly from what is observed for regular nanopores. Depending on the size, length, and number of constrictions in the pores, the filling and emptying processes are found to be of different nature. In every case, these mechanisms involve the coexistence between the confined liquid and some gas nanobubbles that are trapped within the main cavities of the pore. It is also found that the finite length of the pore introduces some

heterogeneity in the adsorption and desorption processes; the filling and emptying of the regions (constriction and cavities) near the pore surface differ from those of the regions in the pore center. Our results show that the condensation and evaporation pressures of the confined fluid significantly depend on the pore morphology (not only on the pore size). This suggests that adsorption isotherms can be used to assess and characterize morphological defects in nanopores, provided that the pore size is known from other independent measurements. One profound finding of this work is that it is very difficult to relate in a quantitative way the morphology and pore sizes to the measured condensation pressures as they depend on all pore characteristics (length, diameter, number of constrictions, etc.). Our results also suggest that microcalorimetry experiments such as measurements of the isosteric heat of adsorption cannot be used to gain information regarding such defects as all of the data for the regular and constricted pores fall on the same curve.

References and Notes

(1) Gelb, L. D.; Gubbins, K. E.; Radhakrishnan R.; Sliwinska-Bartkowiak, M. *Rep. Prog. Phys.* **1999**, *62*, 1573−1659.

(2) Alba-Simionesco, C.; Coasne, B.; Dosseh, G.; Dudziak, G.; Gubbins, K. E.; Radhakrishnan, R.; Sliwinska-Bartkowiak, M. *J. Phys.: Condens. Matter* **2006**, *18*, R15.

(3) Beck, J. S.; Vartulli, J. C.; Roth, W. J.; Leonowicz, M. E.; Kresge, C. T.; Schmitt, K. D.; Chu, C. T.-W.; Olson, D. H.; Sheppard, E. W.; McCullen, S. B.; Higgins, J. B.; Schlenker, J. L. *J. Am. Chem. Soc.* **1992**, *114*, 10834.

(4) Zhao, D.; Feng, J.; Huo, Q.; Melosh, N.; Fredrickson, G. H.; Chmelka, B. F.; Stucky, G. D. *Science* **1998**, *279*, 548.

(5) Corma, A. *Chem. Rev.* **1997**, *97*, 2373.

(6) Ciesla, U.; Schüth, F. *Microporous Mesoporous Mater.* **1999**, *27*, 131.

(7) Soler-Illia, G. J. de A. A.; Sanchez, C.; Lebeau, B.; Patarin, J. *Chem. Rev.* **2002**, *102*, 4093.

(8) Imperor-Clerc, M.; Davidson, P.; Davidson, A. *J. Am. Chem. Soc.* **2000**, *122*, 11925.

(9) Ryoo, R.; Ko, C. H.; Kruk, M.; Antochshuk, V.; Jaroniec, M. *J. Phys. Chem. B* **2000**, *104*, 11465.

(10) Liu, Z.; Terasaki, O.; Ohsuna, T.; Hiraga, K.; Shin, H. J.; Ryoo, R. *Chem. Phys. Chem.* **2001**, *2*, 229.

(11) Galarneau, A.; Cambon, H.; Di, Renzo, F.; Fajula, F. *Langmuir* **2001**, *17*, 8328.

(12) Galarneau, A.; Cambon, H.; Di, Renzo, F.; Ryoo, R.; Choi, M.; Fajula, F. *New J. Chem.* **2003**, *27*, 73.

(13) Liu, Z.; Terasaki, O.; Ohsuna, T.; Hiraga, K.; Shin, H. J.; Ryoo, R. *Chem. Phys. Chem.* **2001**, *4*, 229.

(14) Jun, S.; Joo, S. H.; Ryoo, R.; Kruk, M.; Jaroniec, M.; Liu, Z.; Ohsuna, T.; Terasaki, O. *J. Am. Chem. Soc.* **2000**, *122*, 10712.

(15) Sonwane, C. G.; Bhatia, S. K.; Calos, N. J. *Langmuir* **1999**, *15*, 4603.

(16) Berenguer-Murcia, A.; Garcia-Martinez, J.; Cazorla-Amoros, D.; Martinez-Alonso, A.; Tascon, J. M. D.; Linares-Solano, A. In *Studies in Surface Science and Catalysis;* Rodriguez-Reinoso, F., McEnaney, B., Rouquerol, J., Unger, K., Eds.; Elsevier Science: New York, 2002; Vol. 144, p 83.

(17) Edler, K. J.; Reynolds, P. A.; White, J. W. *J. Phys. Chem. B* **1998**, *102*, 3676.

(18) Everett, D. H. *The Structure and Properties of Porous Materials;* Butterworths: London, 1958; p 95. Barker, J. A. *The Structure and Properties of Porous Materials;* Butterworths: London, 1958; p 125.

(19) Mason, G. *J. Colloid Interface Sci.* **1982**, *88*, 36. Mason, G. *Proc. R. Soc. London A* **1988**, *415*, 453.

(20) Pellenq, R. J.-M.; Levitz, P. E. *Mol. Phys.* **2002**, *100*, 2059−2077.

(21) Coasne, B.; Grosman, A.; Ortega, C.; Pellenq, R. J.-M. In *Studies in Surface Science and Catalysis*; Rodriguez-Reinoso, F., McEnaney, B., Rouquerol, J., Unger, K., Eds.; Elsevier Science: New York, 2002; Vol. 144, p 35.

(22) Coasne, B.; Pellenq, R. J.-M. *J. Chem. Phys.* **2004**, *120*, 2913.

(23) Coasne, B.; Pellenq, R. J.-M. *J. Chem. Phys.* **2004**, *121*, 3767.

(24) Low, M. J. D.; Ramasubramaniam, N. *J. Phys. Chem.* **1967**, *71*, 730.

(25) Huber, T. E.; Huber, C. A. *J. Phys. Chem.* **1990**, *94*, 2505.

(26) Ishikawa, T.; Matsuda, M.; Yasukawa, A.; Kandori, K.; Inagaki, S.; Fukushima, T.; Kondo, S.; *J. Chem. Soc., Faraday Trans.* **1996**, *92*, 1985.

(27) Landmesser, H.; Kosslick, H.; Storek, W.; Frick, R. *Solid State Ionics* **1997**, *101−103*, 271.

(28) Cauvel, A.; Brunel, D.; Di Renzo, F.; Fubini, B.; Garrone, E. *Langmuir* **1997**, *13*, 2773.

(29) Zhao, X. S.; Lu, G. Q.; Whittaker, A. K.; Millar, G. J.; Zhu, H. Y. *J. Phys. Chem. B* **1997**, *101*, 6525.

(30) Sutra, P.; Fajula, F.; Brunel, D.; Lentz, P.; Daelen, G.; Nagy, J. B. *Colloids Surf., A* **1999**, *158*, 21.

(31) Nicholson, D.; Parsonage, N. G. *Computer Simulation and the Statistical Mechanics of Adsorption*; Academic Press: New York, 1982.

(32) Allen, M. P.; Tildesley, D. J. *Computer Simulation of Liquids*; Clarendon Press: Oxford, 1987.

(33) Frenkel, D.; Smit, B. *Understanding Molecular Simulation: From Algorithms to Applications*, 2nd ed.; Academic Press: London, 2002.

(34) Pellenq, R. J.-M.; Nicholson, D. *J. Phys. Chem.* **1994**, *98*, 13339.

(35) Pellenq, R. J.-M.; Nicholson, D. *Langmuir* **1995**, *11*, 1626.

(36) Gelb, L. D.; Gubbins, K. E. *Langmuir* **1998**, *14*, 2097.

(37) Pellenq, R. J.-M.; Levitz, P. E. *Mol. Simul.* **2001**, *27*, 353.

(38) Gelb, L. D. *Mol. Phys.* **2002**, *100*, 2049.

(39) Streett, W. B.; Staveley, L. A. K. *J. Chem. Phys.* **1967**, *47*, 2449.

(40) Kofke, D. A. *J. Chem. Phys.* **1993**, *105*, 4149.

(41) Neimark, A. V.; Ravkovitch, P. I.; Grun, M.; Schuth, F.; Unger, K. K. *J. Colloid Interface Sci.* **1998**, *207*, 159.

(42) Coasne, B.; Galarneau, A.; Di Renzo, F.; Pellenq, R. J.-M. *Langmuir* **2006**, *22*, 11097.

(43) Coasne, B.; Gubbins, K. E.; Pellenq, R. J.-M. *Part. Part. Syst. Char.* **2004**, *21*, 149.

(44) Sarkisov, L.; Monson, P. A. *Langmuir* **2001**, *17*, 7600.

(45) Ravikovitch, P. I.; Neimark, A. V. *Langmuir* **2002**, *18*, 1550.

(46) Vishnyakov, A.; Neimark, A. V. *Langmuir* **2003**, *19*, 3240.

(47) Van Der Voort, P.; Ravikovitch, P. I.; De Jong, K. P.; Benjelloun, M.; Van Bavel, E.; Janssen, A. H.; Neimark, A. V.; Weckhuysen, B. M.; Vansant, E. F. *J. Phys. Chem. B* **2002**, *106*, 5873−5877.

(48) Ravikovitch, P. I.; Neimark, A. V. *Langmuir* **2002**, *18*, 9830−9837.

(49) Maddox, M. W.; Gubbins, K. E. *Langmuir* **1995**, *11*, 3988.

(50) Burgess, C. G. V.; Everett, D. H.; Nuttall, S. *Langmuir* **1990**, *6*, 1734.

(51) Morishige, K.; Fujii, H.; Uga, M.; Kinukawa, D. *Langmuir* **1997**, *13*, 3494.

(52) Morishige, K.; Ito, M. *J. Chem. Phys.* **2002**, *117*, 8036.

(53) Trens, P.; Tanchoux, N.; Galarneau, A.; Brunel, D.; Fubini, B.; Garrone, E.; Fajula, F.; Di Renzo, F. *Langmuir* **2005**, *21*, 8560.

(54) Nakanishi, H.; Fisher, M. *J. Chem. Phys.* **1983**, *78*, 3279.

(55) Evans, R.; Marini Bertollo Marconi, U.; Tarazona, P. *J. Chem. Phys.* **1986**, *84*, 2376.

(56) Ball, P. C.; Evans, R. *Langmuir* **1989**, *5*, 714.

(57) Woo, H. J.; Monson, P. A. *Phys. Rev. E* **2003**, *67*, 041207.

(58) Coasne, B.; Gubbins, K. E.; Pellenq, R. J. M. *Adsorption* **2005**, *11*, 289.

(59) Pellenq, R. J. M.; Coasne, B.; Denoyel, R.; Puibasset, J. In *Studies in Surface Science and Catalysis*; Elsevier Science: New York, 2006, in press.

(60) Ravikovitch, P. I.; Neimark, A. V. *Langmuir* **2002**, *18*, 1550.

(61) Vishnyakov, A.; Neimark, A. V. *Langmuir* **2003**, *19*, 3240.

(62) Libby, B.; Monson, P. A. *Langmuir* **2004**, *20*, 4289.

(63) Detcheverry, F.; Kierlik, E.; Rosinberg, M. L.; Tarjus, G. *Phys. Rev. E* **2003**, *68*, 061504.

(64) Detcheverry, F.; Kierlik, E.; Rosinberg, M. L.; Tarjus, G. *Langmuir* **2004**, *20*, 8006−8014.

(65) Van Der Voort, P.; Ravikovitch, P. I.; De Jong, K. P.; Benjelloun, M.; Van Bavel, E.; Janssen, A. H.; Neimark, A. V.; Weckhuysen, B. M.; Vansant, E. F. *J. Phys. Chem B* **2002**, *106*, 5873.

(66) Ravikovitch, P. I.; Neimark, A. V. *Langmuir* **2002**, *18*, 9230.

(67) Malanoski, A. P.; Van Swol, F. *Phys. Rev. E* **2002**, *66*, 041603.

(68) Kierlik, E.; Rosinberg, M. L.; Tarjus, G.; Viot, P. *Phys. Chem. Chem. Phys.* **2001**, *3*, 1201.

(69) Kierlik, E.; Monson, P. A.; Rosinberg, M. L.; Sarkisov, L.; Tarjus, G. *Phys. Rev. Lett.* **2001**, *87*, 055701.

(70) Kierlik, E.; Monson, P. A.; Rosinberg, M. L.; Tarjus, G. *J. Phys.: Condens. Matter* **2002**, *14*, 9295.

(71) Brown, A. J. Ph.D. Thesis, University of Bristol, 1963.

(72) Gelb, L. D.; Gubbins, K. E. *Langmuir* **1999**, *15*, 305.

(73) Pellenq, R. J. M.; Rodts, S.; Pasquier, V.; Delville, A.; Levitz, P. *Adsorption* **2000**, *6*, 241.

(74) Bock, H.; Schoen, M. *Phys. Rev. E* **1999**, *59*, 4122.

(75) Bock, H.; Diestler, D. J.; Schoen, M. *J. Phys.: Condens. Matter* **2001**, *13*, 4697.

(76) Puibasset, J. *J. Phys. Chem. B* **2005**, *109*, 4700.

(77) Puibasset, J. *J. Phys. Chem. B* **2005**, *109*, 8185.

(78) Puibasset, J. *J. Chem. Phys.* **2006**, *125*, 074707.

(79) Kuchta, B.; Llewellyn, P.; Denoyel, R.; Firlej, L. *Colloids Surf., A* **2004**, *241*, 137.